



# Evolution of magma decompression and discharge during a Plinian event (Late Bronze-Age eruption, Santorini) from multiple eruption-intensity proxies

Madison L. Myers<sup>1,2</sup> · Timothy H. Druitt<sup>1</sup> · Federica Schiavi<sup>1</sup> · Lucia Gurioli<sup>1</sup> · Taya Flaherty<sup>1</sup>

Received: 10 August 2020 / Accepted: 14 January 2021  
© International Association of Volcanology & Chemistry of the Earth's Interior 2021

## Abstract

We have coupled three independent methods to investigate the time evolution of eruptive intensity during the sub-Plinian and Plinian phases of the 3600-year BP Late Bronze-Age eruption of Santorini Volcano: (1) mass eruption rate based on new lithic isopleth maps for multiple layers of the fall deposit, (2) magma decompression rate calculated from vesicle number densities, and (3) magma decompression rate calculated from  $H_2O$  gradients in melt reentrants, with methods 2 and 3 measured on the same suite of pyroclasts. Mass eruption rate increased by two orders of magnitude, reaching  $210 \times 10^6 \text{ kg s}^{-1}$  at the peak of the Plinian phase (plume height  $28.4 \pm 1.0 \text{ km}$ ); it then declined in the final stage of fallout emplacement following the first generation of pyroclastic surges. Decompression rates from melt reentrants ( $0.008$  to  $0.25 \text{ MPa s}^{-1}$ ) are two to three orders of magnitude lower than those from vesicle number densities, assuming heterogeneous vesicle nucleation ( $2$  to  $19 \text{ MPa s}^{-1}$ ). Melt reentrants are thought to record slow decompression in the deep feeder conduit, whereas vesicles record much higher rates of decompression in the shallow conduit due to the steep, nonlinear pressure gradients associated with magma vesiculation and fragmentation. Upwardly converging flow from a dike-like, deep conduit to a more cylindrical, shallow conduit may also have played a role in causing upwardly accelerating flow. Variations in deep decompression rate recorded by melt reentrants are decoupled from mass eruption rate, whereas those recorded by vesicles lie in between. Taken with the transition from unsteady to steady Plinian eruption, this may reflect the existence of transient flow conditions in the conduit system due to widening and lengthening of a deep feeder dike as Plinian eruption progressed. As the mass eruption rate rose to its peak value, the fragmentation level fell in the conduit due to increasing rates of magma strain and decompression.

**Keywords** Plinian eruption · Santorini · Decompression rate · Conduit development · Vesicle number density · Melt reentrant

## Introduction

Caldera-forming explosive eruptions are amongst the most devastating natural events on Earth (Mason et al. 2004; Miller and Wark 2008). As more than 500 million people live within the maximum exposure range of a volcano (Doocy et al. 2013), refining techniques to measure how quickly

magma moves to the surface, and how magma flow evolves over the course of an eruption, is crucial for improved hazard monitoring and risk mitigation. Determining the processes that control transitions in eruption style, which commonly take place during eruptions due to shifts in external and internal parameters, is also important (Hildreth and Drake 1992; Woods and Koyaguchi 1994; Castro and Gardner 2008; Degruyter et al. 2012). Few silicic caldera-forming eruptions have ever been recorded by modern scientific instrumentation, so understanding of the processes leading up to, and during, such eruptions relies heavily on studies of their erupted products.

Three main clast-based techniques are available for estimating magma flow rate from measurements on pyroclastic fall deposits. One uses clast-isopleth data to estimate eruption plume height through application of plume model inversions (Carey and Sparks 1986; Bonadonna and Costa 2013). By

Editorial responsibility: R. Cioni; Deputy Executive Editor: J. Tadeucci

✉ Madison L. Myers  
madison.myers@montana.edu

<sup>1</sup> CNRS, IRD, OPGC, Laboratoire Magmas et Volcans, Université Clermont Auvergne, F-63000 Clermont-Ferrand, France

<sup>2</sup> Department of Earth Sciences, Montana State University, Bozeman, MT 59717-1272, USA

splitting the fall deposit into multiple layers, this technique can yield variations of mass eruption rate with time (Sulpizio et al. 2010; Houghton et al. 2014). Decompression rates for particular volcanic episodes can also be determined using individual pyroclasts. For instance, the number density of vesicles generated by ascent-driven nucleation is a function of magma decompression rate (e.g., Klug and Cashman 1996; Mourtada-Bonnefoi and Laporte 2004; Massol and Koyaguchi 2005; Toramaru 2006; Cluzel et al. 2008; Shea et al. 2010; Giachetti et al. 2010; Hamada et al. 2010; Martel and Iacono-Marziano 2015; Hajimirza et al. 2019; Nishiwaki and Toramaru 2019), although several processes occur in the conduit (e.g., heterogeneous nucleation and coalescence) that may complicate interpretation. Another approach is to model gradients of dissolved  $H_2O$  and (if present in detectable quantities)  $CO_2$  preserved in crystal-hosted melt reentrants to estimate the decompression rate experienced by the crystal during ascent to the surface and prior to eruption quench (Liu et al. 2007; Myers et al. 2016, 2018). Although several studies have investigated the evolution of mass eruption rate with vesicle number density (and calculated decompression rate) through a volcanic sequence, no study has directly compared decompression rates determined using melt reentrants with those using vesicle number density from the same pyroclasts.

In this study we compare and contrast all three independent methods during the opening sub-Plinian and Plinian fallout phases of the Late Bronze-Age (LBA) eruption of Santorini (Bond and Sparks 1976; Taddeucci and Wohletz 2001; Druitt 2014). We integrate the results with pre-existing interpretations for how eruptive activity proceeded during these eruptive phases. A major conclusion of our work is that decompression rates recorded by the deep and shallow conduit systems are decoupled, and we propose a possible explanation in the case of the LBA eruption.

## Geologic background

The Santorini volcanic field is located on the Aegean volcanic arc, within a NE-SW trending rift zone (Fig. 1a). It is the most active volcanic center in the eastern Mediterranean region, having had at least twelve Plinian eruptions over the last 360 ky, interspersed with episodes of lava emission and smaller explosive events (Druitt et al. 1999). The present-day (LBA) caldera is up to 400 m deep and is cut by a prominent NE-SW lineament called the Kameni Line, which is parallel to the rift zone (Fig. 1b). Vents of historical volcanic activity are aligned along the Kameni Line, as were epicenters of the seismic unrest of 2011–2012 (Kaviris et al. 2015), highlighting that it is a major line of weakness in the caldera.

The LBA eruption (also commonly called the Minoan eruption) was the most recent Plinian event at Santorini, occurring  $\sim 3600$  years ago. It discharged  $48\text{--}86\text{ km}^3$  of magma

and comminuted rock debris, and collapsed a large part of the modern-day caldera. It began with sub-Plinian precursory explosions, the plumes from which were largely dispersed to the south (phase 0) (Heiken and McCoy 1990; Cioni et al. 2000). The eruption then evolved through four main phases (Fig. 1c): a Plinian plume (phase 1); pyroclastic surges (phase 2); low-temperature pyroclastic flows (phase 3); and voluminous hot, fluidized pyroclastic flows (phase 4) (Bond and Sparks 1976; Heiken and McCoy Jr 1984; Sparks and Wilson 1990; Taddeucci and Wohletz 2001; Druitt 2014).

The vent for phase 1 has been extrapolated to a location on the Kameni Line; the plume was dispersed to the east to south-east and grew with time, producing a reversely graded pumice fall deposit preserved up to 6 m thick (Bond and Sparks 1976; Heiken and McCoy Jr 1984). The resulting fall deposit has a volume of at least  $1\text{--}2\text{-km}^3$  dense-rock equivalent, and has been subdivided into four layers, P1a–P1d (Druitt 2014). Layer P1a is crudely stratified and records an initial, unsteady Plinian plume; layer P1b is non-stratified and records a steadier plume. Layer P1c is a thin pyroclastic surge bed (commonly referred to in previous publications as the “phreatomagmatic break” or “flow break”); it is overlain by layer P1d, the last fall layer prior to the transition to eruptive phase 2 (Figs. 1c and 2c, d).

In this paper we focus solely on the fall deposits of phases 0 and 1. Juvenile pyroclasts in these phases are white rhyodacite pumices, microphenocryst-rich andesitic pumices, and (in the upper portion P1b) cauliform andesitic enclaves. Although the rhyodacite pumices account for  $> 99\%$  of all LBA magma erupted, microphenocryst-rich pumices can comprise 40–90% of the juvenile material in P0 and the lower levels of P1 (see Table 1 from Druitt 2014). The influx of cauliform andesitic enclaves occurs part way up layer P1b, with their size increasing in conjunction with those of the rhyodacitic pumices and lithic clasts. The microphenocryst-rich pumices and cauliform andesitic enclaves are inferred to represent a separate magma intrusion that was intersected during the tapping of the main rhyodacitic reservoir (Druitt 2014). In this study we focus on the rhyodacitic pumices, and the cauliform enclaves and microphenocryst-rich pumices are not considered. Previous work of Wilson and Houghton (1990) noted only a slight decrease in rhyodacitic pumice density ( $\sim 0.6$  to  $\sim 0.5\text{ kg/m}^3$ ), and overall consistent vesicularity (73–82%), upwards through P1.

Lithic components in the LBA fallout units have been interpreted to record changing levels of fragmentation with time (Druitt 2014). Lithics in P0 and at the base of P1 are dominated by lavas, inferred to be shallowly derived. About mid-way through P1b, the proportion of altered lava lithics increases, and hydrothermally iron-stained blocks of holocrystalline to glass-bearing granitoids appear in abundance (Figs. 1c and 2b). These then increase in size and abundance to the top of P1b, where they account for a third of the

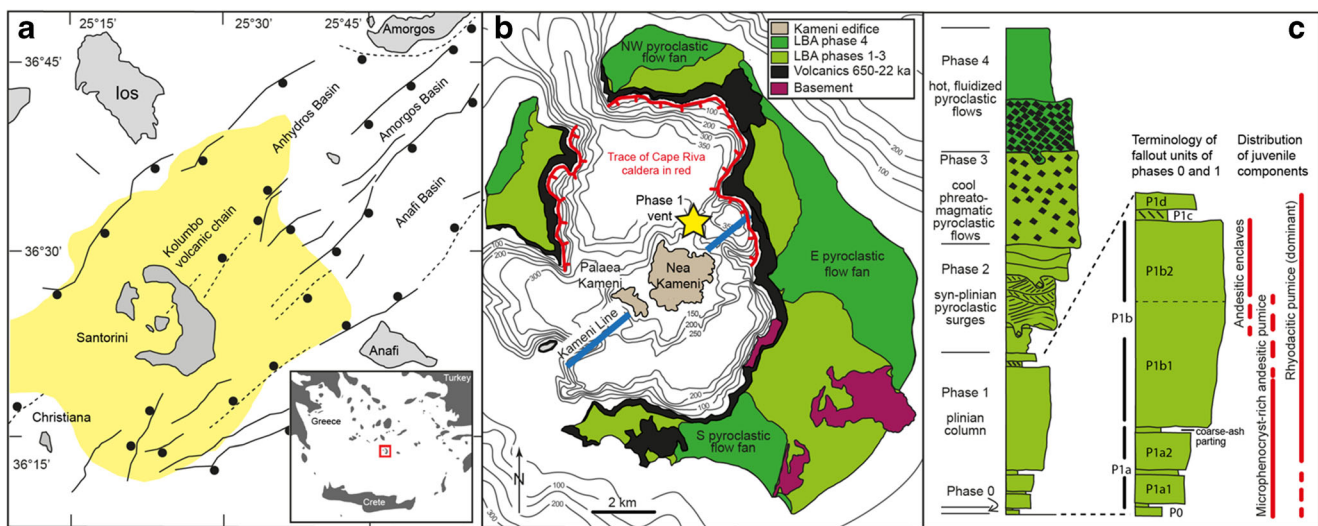


**Fig. 1** Summary of geological features of Santorini and the Late Bronze-Age (LBA) eruption after Flaherty et al. (2018) and references therein. **a** Map of Santorini and its host rift zone, showing major normal faults (circle on the hanging wall), and the three main subsidence basins. The extent of submarine ignimbrite from the LBA eruption mapped from seismic profiles is shown in yellow. A location map is included as inset.

**b** Map of Santorini caldera, showing the products of the LBA eruption (including the three main ignimbrite fans from eruptive phase 4), the outline of the shallow Cape Riva caldera that existed prior to the LBA eruption, the Kameni Line, and the approximate location of the Plinian vent. **c** Schematic log of the products of the LBA eruption, with the distributions of the juvenile components after Druitt 2014

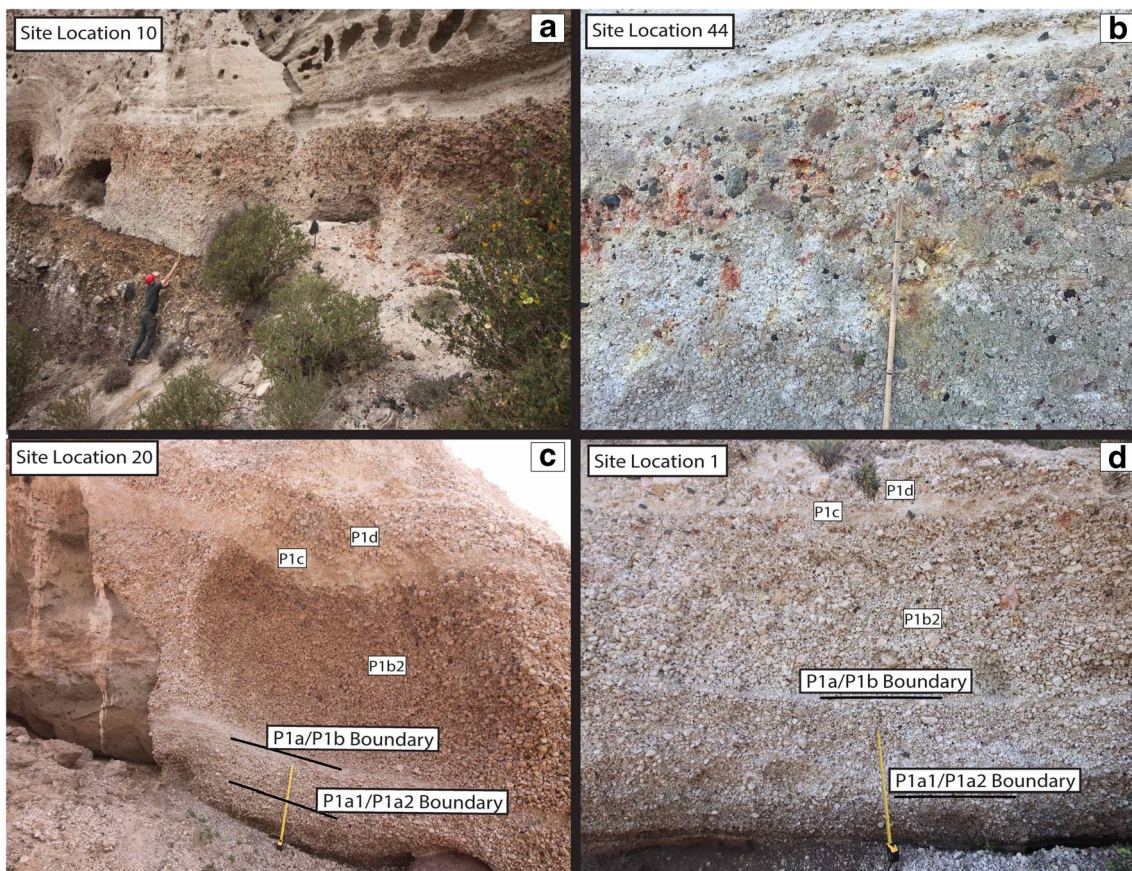


**Fig. 2** Field photos of the Plinian pumice fall deposit of phase 1 (P1) of the eruption, with a meter stick represented in each photo. **a** The pumice fall deposit overlying breccias from an earlier eruption, and itself overlain by the bedded tuffs of phase 2. **b** The top of P1 showing the abundance of hydrothermally stained granitoid clasts at this level. **c, d** The P1 pumice

fall deposit in southern Santorini where layer P1b is underlain by layer P1a, with a coarse ash separating the two. The thin lapilli fallout of P0 lies at the bases of these outcrops. GPS locations for each site can be found in Supplementary Table 1.

**Table 1** Descriptions of each of the six fallout layers and parameters calculated from lithic isopleth maps

Layer	Characteristics	Plume height (km) <sup>a</sup>	Wind direction	MER (kg/s) <sup>b</sup>	MER (kg/s) <sup>c</sup>
P0	Coarse ash fall with some microphenocryst-rich pumices. Beds A of Cioni et al. (2000)	8.5 ± 1.54	S	1.7 ± 1.2 × 10 <sup>6</sup>	1.0 × 10 <sup>6</sup>
P1a1	Lapilli pumice fall with abundant microphenocryst-rich pumices. Reversely graded. Gray coloring	11.6 ± 2.1	SSE	5.8 ± 3.9 × 10 <sup>6</sup>	3.7 × 10 <sup>6</sup>
P1a2	Lapilli pumice fall with abundant microphenocryst-rich pumices. Two reversely zoned layers. Gray coloring	14.3 ± 1.1	SE	1.3 ± 0.4 × 10 <sup>7</sup>	8.8 × 10 <sup>6</sup>
P1b1	Pumice fall deposit with whiter appearance. Microphenocryst-rich pumices scarce	18.0 ± 1.3	E, SE	3.4 ± 1.1 × 10 <sup>7</sup>	2.3 × 10 <sup>7</sup>
P1b2	Pumice fall deposit with white appearance. Microphenocryst-rich pumices scarce. P1b1/P1b2 boundary marked by incoming of rare cauliform andesitic scoria.	28.4 ± 1.0	NE, E	2.1 ± 0.6 × 10 <sup>8</sup>	1.5 × 10 <sup>8</sup>
P1d	Following pyroclastic surge deposit (P1c), final pumice fall layer before passage to P2	21.7 ± 1.1	No wind?	7.2 ± 1.3 × 10 <sup>7</sup>	5.0 × 10 <sup>7</sup>

\*The plume height presented is determined using the 3.2-cm isopleth, assuming a lithic density of 2500 kg/m<sup>3</sup>, and calculated using the plume inversion model of Carey and Sparks (1986), except for P0, where we used the value of Cioni et al. (2000). For each layer, the minimum and maximum plume height was determined based on uncertainties in the cross- and downwind ranges; the average of this range is presented here along with the estimated uncertainty. Mass eruption rate (MER) was estimated using the methods of Wilson and Walker (1987) and Mastin et al. (2009), and the uncertainty estimated for the Wilson and Walker (1987) value

<sup>a</sup> Carey and Sparks (1986)

<sup>b</sup> Wilson and Walker (1987)

<sup>c</sup> Mastin et al. (2009)

lithic assemblage. Following the first pyroclastic surge (P1c), the final fall layer (P1d) is again dominated by fresh lavas. Making the assumption that free lithics are derived from or above the fragmentation level (e.g., Barberi et al. 1989), the data indicate that the magma fragmentation level was shallow during phase P1a, then descended with time, reaching the top of melt-bearing plutonic lithologies towards the end of phase P1b.

Phase equilibria experiments and melt inclusion volatile contents have constrained the pre-eruptive storage conditions of the ~ 70 wt% SiO<sub>2</sub> rhyodacite to 850–880 °C, 100–160 MPa, 4–5 wt% H<sub>2</sub>O, and < 200 ppm CO<sub>2</sub> (Cottrell et al. 1999; Cadoux et al. 2014; Druitt et al. 2016; Flaherty et al. 2018).

## Methods

We divided the fall deposit into six layers, expanding upon the original four: P0, P1a1, P1a2, P1b1, P1b2, and P1d (Figs. 1c and Fig. 2). Layer P1a1 is defined by two reversely zoned units, with the transition to P1a2 marked by a coarsening of grain size (Fig. 2c, d). A thin parting of coarse ash separates layers P1a2 and P1b1, indicating a transient lowering of the eruption plume. The boundary between P1b1 and P1b2 is identified by the first appearance of cauliform andesitic enclaves. The six layers could be traced between multiple sites around the caldera rim. Maximum lithic size and fall layer thickness measurements were made at 43 localities (see

Supplementary Table 1) to determine the evolution of plume height, wind direction, and mass eruption rate during phases 0 and 1, following the methods of Carey and Sparks (1986). For each site, layer thickness was measured at several local sections, and an average was used on the isopach map (Fig. 3). Following the recommendations of Biass and Bonadonna (2011), three dimensions of the five largest lithic clasts from a 1-m<sup>2</sup> section were measured for each fall layer, and the mean of these five averaged diameters was used to create a lithic isopleth map (Supplementary Table 1). Thickness and lithic measurements for P0 were presented previously by Cioni et al. (2000). We use their estimate for phase 0 plume height and convert it to mass eruption rate in the same way as for our phase 1 data (see Table 1).

Single pumice clasts were collected from within each of the six fall layers, with three samples collected from the thick P1b (lower, middle, upper), resulting in eight samples for this study—one in P0 and seven in P1 (Supplementary Table 2). Given the restricted range of pumice vesicularity and density (Wilson and Houghton 1990), no particular clast density class was targeted. All samples from P1 were analyzed for melt reentrants and vesicle number density from single pumice clasts; P0 pumices are significantly smaller (< 5 cm) than those of P1 used in this study (6–13 cm: Supplementary Table 2), requiring multiple clasts to be crushed to obtain enough crystals to find melt reentrants. The pumices were scrubbed to remove any adhering ash matrix, and to ensure that microphenocryst-rich pumices were avoided, as they may have had a different decompression history. Effort was made

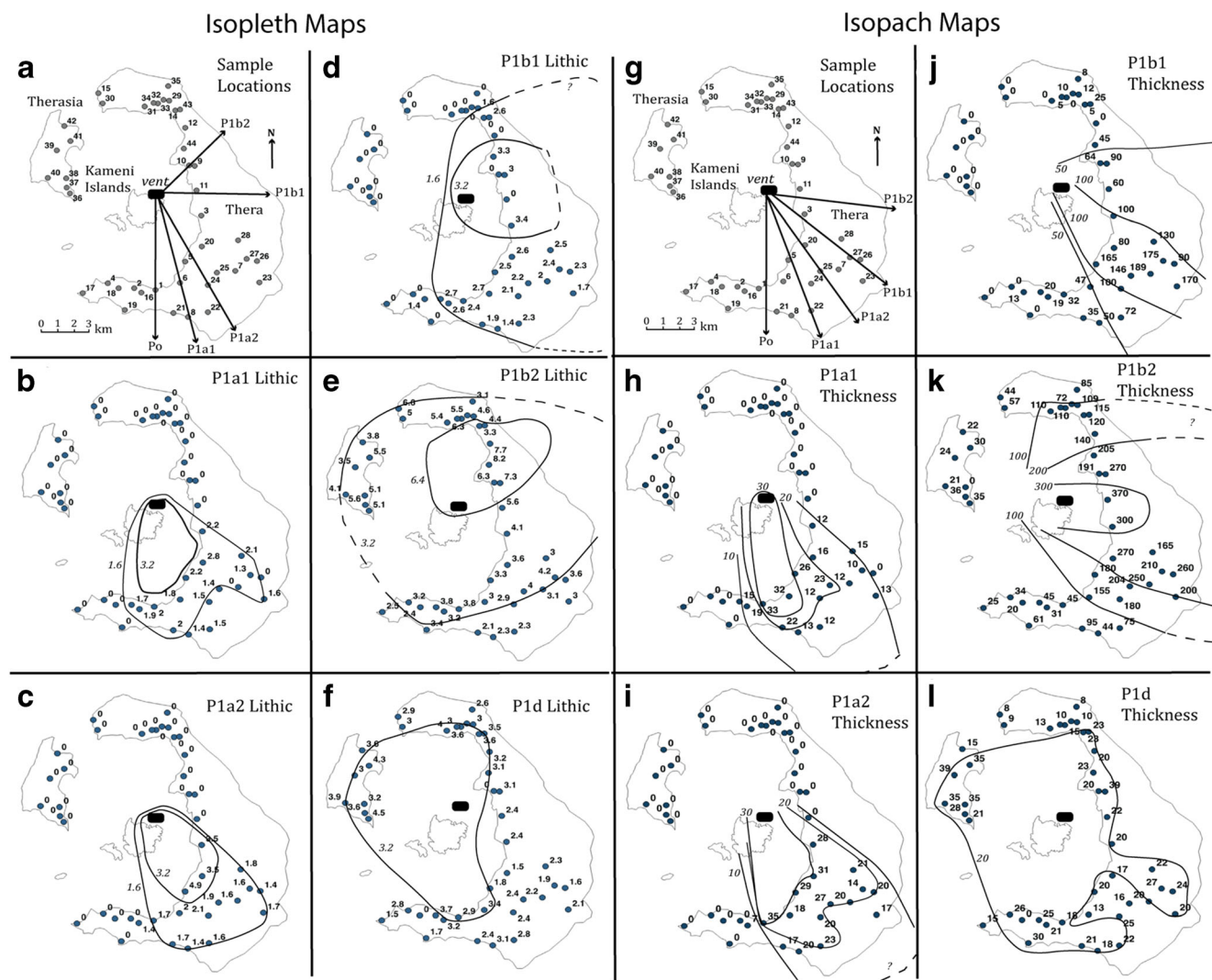


**Fig. 3** Thickness and maximum lithic size data from 43 sample locations. **a–f** Isopleth data (mean diameter in cm of three axes of the five largest lithic fragments in  $1\text{ m}^2$  of each layer). **g–l** Isopach data (cm). Figures (a) and (g) summarize the wind directions inferred from each technique. P0

wind direction was taken from Cioni et al. (2000). The implied source vent for the eruption is shown by the black dot, matching that of Bond and Sparks (1976)

to avoid pumices with strongly elongated vesicles (Taddeucci and Wohletz 2001), which would affect estimation of vesicle number density. For vesicle analysis, we chose to focus on the rim of each pumice clast, as rims are less likely to have been affected by post-fragmentation vesicle growth and coalescence (Thomas et al. 1994; Shea et al. 2010). Vesicle number densities from thick sections of pumice rims were imaged using a scanning electron microscope at image magnifications from  $\times 25$  up to  $\times 1000$ , and then quantified by analyzing six  $\times 500$  and two  $\times 1000$  images per pumice clast in FOAMS (Shea et al. 2010). The choice of analyzing these two high magnifications serves to focus our counting on the smallest vesicles, which dominate vesicle number density (Houghton et al. 2010). In our calculations, we assumed a constant vesicularity of 75%, based upon the relatively homogenous vesicularity data of Wilson and Houghton (1990). Full processing

procedures and discussion of error can be found in the Supplementary Material.

The remaining portions of each pumice clast were crushed using a mortar and pestle, sieved to 250- and 500- $\mu\text{m}$  size fractions, and picked for plagioclase, clinopyroxene, and orthopyroxene. All selected crystals were coated in vesiculated glass (Supplementary Figure 1). The crystal separates were then submerged in isopropyl alcohol to search for melt reentrants. This method worked well for plagioclase, but for the darker pyroxenes, it was commonly necessary to mount the crystals in Crystalbond, slightly polish into their interiors, and use an optical microscope to search for melt reentrants. Plagioclase was found to contain the majority of melt reentrants (perhaps due to the challenge of observing them in the pyroxene), mostly situated on crystal faces. Due to the requirements of the 1D diffusion code, care was taken to select only

those rare melt reentrants with a simple morphology (i.e., no bottleneck, internal vesicles or minerals, multiple tubes, etc.), which would complicate diffusion assumptions (Supplementary Figure 2). We also selected reentrants with a single vesicle at their mouths to ensure efficient diffusive exchange between the reentrant and the degassing, external melt (after Lloyd et al. 2014). Using this criterion, only a few melt reentrants were found per 50–100 crystals, although this was quite variable between layers. Sixteen melt reentrants in total were studied (Fig. 4): fourteen in plagioclase, one in orthopyroxene, and one in clinopyroxene. All melt reentrants were measured along their lengths (ranging from 80 to 320  $\mu\text{m}$ ) for  $\text{H}_2\text{O}$  and  $\text{CO}_2$  concentrations using a Thermo-Nicolet Nexus 670 Fourier transform infrared spectrometer (FTIR) interfaced with a continuum IR microscope at the University of Oregon. Of these sixteen melt reentrants, five were found to have flat profiles and were not able to be fit using the diffusion model; these reentrants were not further evaluated. Following the FTIR analysis at the University of Oregon (FTIR-UO), eight of the eleven melt reentrants were re-analyzed (3 were lost in this process) at the University Clermont Auvergne by FTIR (FTIR-UCA) and Raman spectroscopy (Raman-UCA). This allowed us to evaluate the dependence of modeled

decompression rates on the measured profiles. All methods for these three separate instruments, and detailed transect information, can be found in the Supplementary Material.

To model the measured  $\text{H}_2\text{O}$  diffusion profiles, we applied the 1D constant decompression model of Myers et al. (2018). This model, based on that of Liu et al. (2007), allows for the comparison of the measured and simulated profiles for various decompression rates. The boundary condition at the contact between the host melt and the mouth of the melt reentrant is based on the melt  $\text{H}_2\text{O}$  and  $\text{CO}_2$  solubility at a given pressure, updated at each decompression step, and is assumed to be in equilibrium with the external melt outside the crystal (Liu et al. 2007; Myers et al. 2016, 2018).

## Results

### Plume heights and mass eruption rates

Isopach and lithic isopleth maps for phase P1 are shown on Fig. 3. The broadening of isopleths upwards in the fall deposit (Fig. 3b–f) records an increase in plume height with time (particularly between P1b1 and P1b2), prior to a decrease in

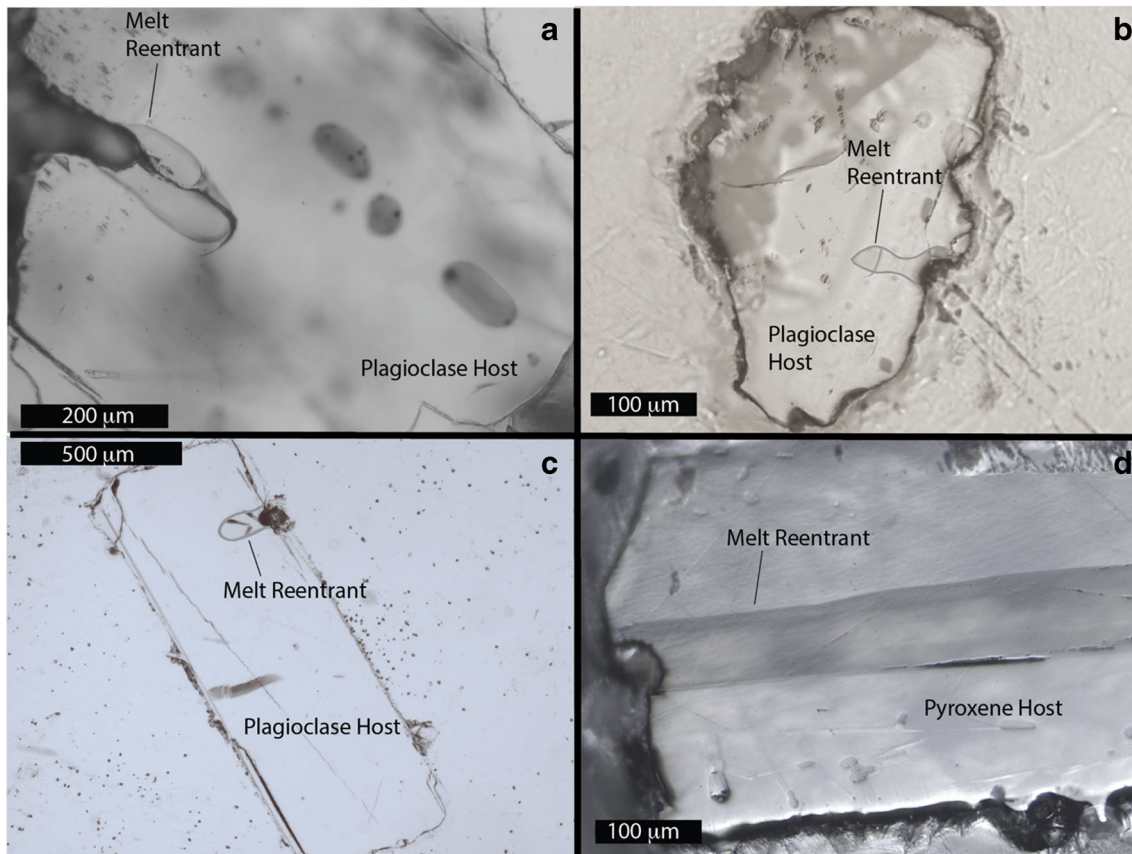


**Fig. 4** Photomicrographs of melt reentrants exposed in plagioclase (a–c) and pyroxene (d) crystals. All melt reentrants clearly display a bubble at their mouth, a requirement to ensure that efficient diffusive exchange is

occurring between the reentrant and surrounding melt. Simple morphologies that lacked strong bottlenecks were chosen in order to validate the 1D assumption

P1d. Wind direction recorded by the isopleths changes from SSE-wards in P1a1 and P1a2, to E-wards in P1b1, to NE-wards in P1b2. Layer P1d appears to have little wind influence on its dispersion. Wind directions recorded by isopach maps of the same levels agree with those for the isopleths for P1a, but disagree for P1b, where isopach wind directions are less rotated than those indicated by the isopleths (Fig. 3a vs. g). This could be due to the fact that each fallout layer is integrating an overall increase in eruption intensity throughout its thickness, so that the upper portion of the layer is probably where the largest clasts reside. Essentially, where the isopleths are recording the wind direction of the upper portion of any given layer, the isopach thickness is averaging the wind direction of that entire layer.

Plume heights for each layer are estimated using the Carey and Sparks (1986) inversion model (Table 1 and Fig. 5). As the height estimate is based solely on the crosswind range (half width of the depositional envelope), uncertainties presented for plume height are based on the “wiggle-room” available in the crosswind range isopleth placement (Fig. 3).

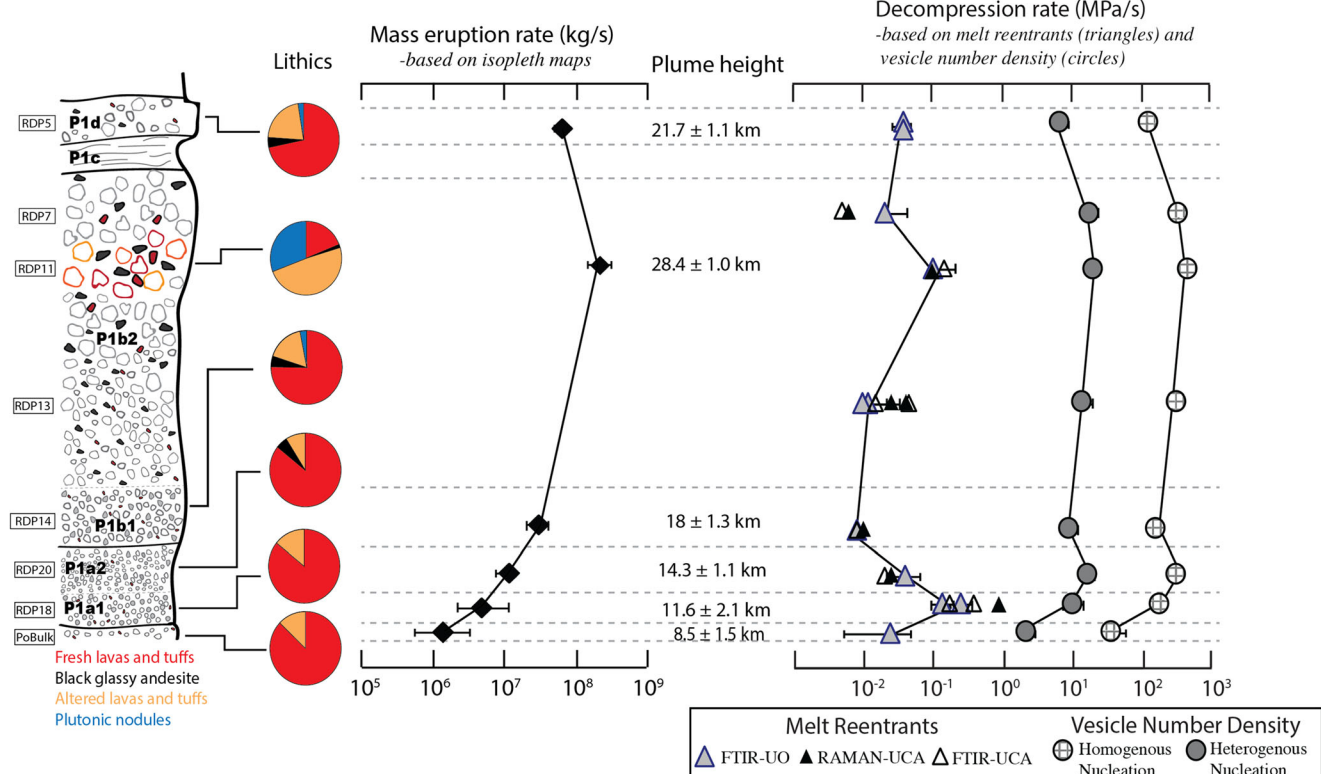
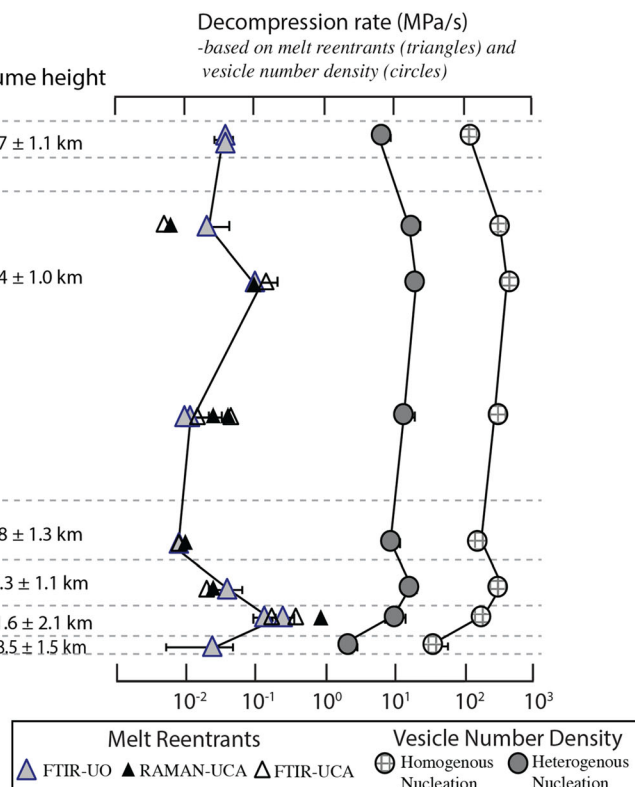


**Fig. 5** Simplified stratigraphy of the deposits from phases 0 (P0) and 1 (P1) of the eruption. Eight pumice samples (names shown in boxes) were taken from six layers (labeled in bold), with the lithic population percentages from Druitt (2014) shown as pie diagrams. Plume heights were calculated using the Carey and Sparks (1986) model from the isopleth data in Fig. 3. Errors in plume height are based on uncertainties in isoline drawing. Plume heights were converted to mass eruption rate using the formula of Wilson and Walker (1987). Decompression rates ( $\text{MPa s}^{-1}$ ) are presented for melt reentrants (triangles), based on modeling of diffusion gradients preserved in plagioclase and pyroxene-hosted melt

Conversion of isopleth data to plume height used the 3.2-cm contour, the only one available for all five layers, although this is loosely constrained for P1a1 and P1a2 (Fig. 3). Plume height estimates were also made for the few other isopleths available; however, agreement is typically poor between conversions (Supplementary Figures 3 and 4). Although it is feasible to take an average plume height based on several isopleths, this can only be completed for certain layers with quality of isopleths not all being equal. We have therefore chosen to focus our interpretations on the 3.2 cm isopleth. Taking  $8.5 \pm 1.5$  km as the estimated plume height for P0 (Cioni et al. 2000), the 3.2-cm isopleths suggest an initial increase in plume height, with the greatest height of  $28.4 \pm 1.0$  km reached in P1b2, decreasing to  $21.7 \pm 1.1$  km in P1d, following initial pyroclastic surge (P1c) production (Fig. 5, Supplemental Figure 4).

Plume heights were converted to mass eruption rate using the methods of Wilson and Walker (1987) and Mastin et al. (2009), yielding values of  $1.7 \times 10^6$  to  $2.1 \times 10^8 \text{ kg s}^{-1}$  and  $1.0 \times 10^6$  to  $1.5 \times 10^8 \text{ kg s}^{-1}$ , respectively (Table 1). Error bars



reentrants, and vesicle number densities (circles). Melt reentrant profiles were measured by FTIR spectroscopy at the University of Oregon (gray triangle), and by FTIR (open triangle) and Raman (black triangle) spectroscopy at the University of Clermont Auvergne. Vesicle number densities were converted to decompression rates using the formula of Toramaru (2006), based on the assumption of either heterogeneous (gray circle) or homogenous (+ circle) vesicle nucleation. Error bars for melt reentrant-based decompression rates are based on the goodness of fit for the modeled profiles

associated with the Wilson and Walker (1987) estimates are propagated based on those determined for each plume height (Table 1). Although the conversion based on the Wilson and Walker (1987) formula is consistently higher, it falls within error of the Mastin et al. (2009) value (Table 1). Importantly, the relative range of two orders of magnitude represented by P0 and P1 is consistent between the two methods. The lowest mass eruption rate is associated with P0, and the highest with P1b2 (Fig. 5).

## Decompression rates from pumice vesicle number densities

Visually, there is a noticeable change in the sizes of vesicles in the rims of pumice clasts up through P0 and P1, with smaller (average diameter 4–5  $\mu\text{m}$ ) vesicles found at the top of P1a and the top of P1b (Fig. 6, Table 2). The largest vesicles, with average diameters of 9–13  $\mu\text{m}$ , are observed in P0 (largest), at the base of P1a, at the base of P1b, and in P1d. Pumice-rim

**Fig. 6** Scanning electron microscope images, all taken at  $\times 500$ , of the eight pumice samples imaged, representing six layers of the pumice fall deposits; three pumice clasts are taken from layer P1b2. The glass is shown in white, and the vesicles in black on each image. Yellow scale in the bottom right corner is 100  $\mu\text{m}$

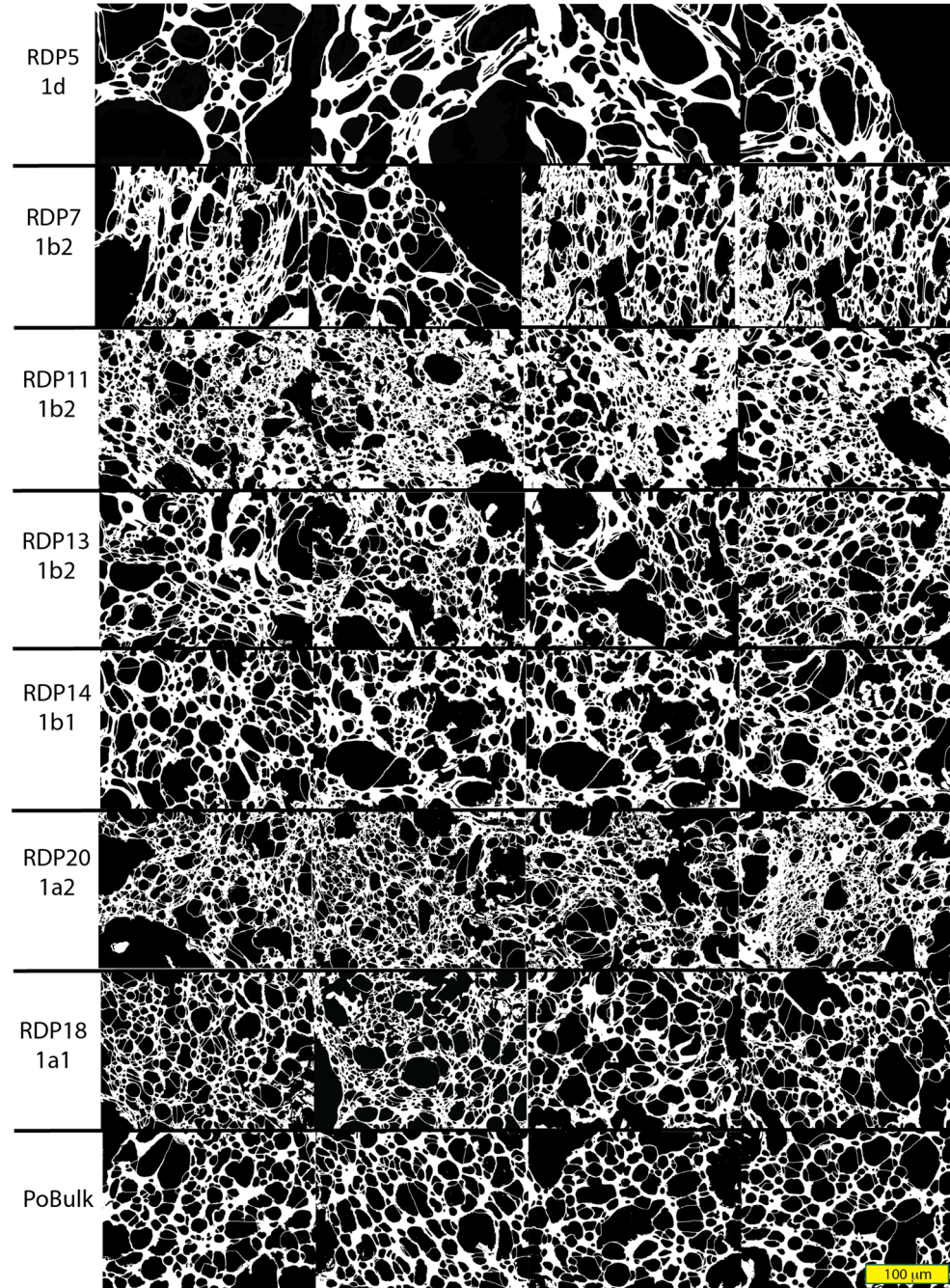


**Table 2** Vesicle size distribution parameters for each pumice clast analyzed

Sample	Location	Fall layer	Average vesicle diameter ( $\mu\text{m}$ ) <sup>a</sup>	$N_V$ ( $\text{mm}^{-3}$ )	$N_V$ <sup>b</sup> corrected ( $\text{mm}^{-3}$ )	$N_V$ <sup>c</sup> uncertainty ( $\text{mm}^{-3}$ )	$dP/dt$ <sup>d</sup> heterog. (MPa/s)	$dP/dt$ <sup>d</sup> homog. (MPa/s)
P0	Location 1	P0	13	$6.24 \times 10^5$	$2.50 \times 10^6$	$7.58 \times 10^5$	2	50
RDP18	Location 1	P1a1	12	$6.43 \times 10^6$	$2.57 \times 10^7$	$1.26 \times 10^7$	11	240
RDP20	Location 1	P1a2	4	$1.45 \times 10^7$	$5.78 \times 10^7$	$9.04 \times 10^6$	17	420
RDP14	Location 11	P1b1	9	$5.37 \times 10^6$	$2.15 \times 10^7$	$5.94 \times 10^6$	9	220
RDP13	Location 11	P1b2	7	$1.07 \times 10^7$	$4.28 \times 10^7$	$1.68 \times 10^7$	15	340
RDP11	Location 11	P1b2	5	$1.64 \times 10^7$	$6.56 \times 10^7$	$1.50 \times 10^7$	19	450
RDP7	Location 11	P1b2	8	$1.56 \times 10^7$	$6.26 \times 10^7$	$1.77 \times 10^7$	19	440
RDP5	Location 11	P1d	9	$3.42 \times 10^6$	$1.37 \times 10^7$	$4.16 \times 10^6$	7	160

<sup>a</sup> Vesicle diameter is an average of the two axes

<sup>b</sup> Vesicle number density ( $N_V$ ) is corrected based on a vesicularity of 75%, taken from Wilson and Houghton (1990)

<sup>c</sup>  $N_V$  uncertainty is based on the 1 sigma SD of the  $N_V$  determined by analyzing each  $\times 500$  image individually

<sup>d</sup> Magma decompression rates ( $dP/dt$ ) were calculated from  $N_V$  using the equations from Toramaru (2006), using assumptions of both heterogeneous and homogenous nucleation

vesicle number density values span 1.5 orders of magnitude, from  $2.50 \times 10^6$  to  $6.56 \times 10^7 \text{ mm}^{-3}$ , falling within the range typical for explosive rhyolitic eruptions (Giachetti et al. 2010; Houghton et al. 2010). The lowest vesicle number density is from P0, and the highest is from P1b2.

Vesicle number densities were converted to decompression rates using Eq. (2) from Toramaru (2006). This requires estimates of the interfacial tension between  $\text{H}_2\text{O}$  and melt, the starting saturation pressure and temperature, and the melt  $\text{H}_2\text{O}$  diffusivity, where the largest uncertainty comes from the choice of interfacial tension (Shea 2017). Using a temperature (850 °C), pressure (165 MPa), and  $\text{H}_2\text{O}$  content (5.2 wt%) appropriate for the LBA magma (Druitt et al. 2016; Flaherty et al. 2018), the diffusivity of  $\text{H}_2\text{O}$  is found to be  $1.1 \times 10^{-11} \text{ m}^2 \text{ s}^{-1}$  (Eq. 27 from Zhang et al. 2007). The only remaining unknown is the interfacial tension, which relies on whether vesicle nucleation was homogenous or heterogeneous. We estimate decompression rates using both nucleation mechanisms, where the interfacial tension is taken to be  $0.025 \text{ N m}^{-1}$  and  $0.12 \text{ N m}^{-1}$  for heterogeneous and homogeneous nucleation, respectively (Shea 2017). Resulting decompression rates recorded by the vesicle number densities are 2–19 MPa  $\text{s}^{-1}$  (heterogeneous) or 50–450 MPa  $\text{s}^{-1}$  (homogeneous). In each case, the lowest rate is from P0 and the highest is from P1b2 (Fig. 5).

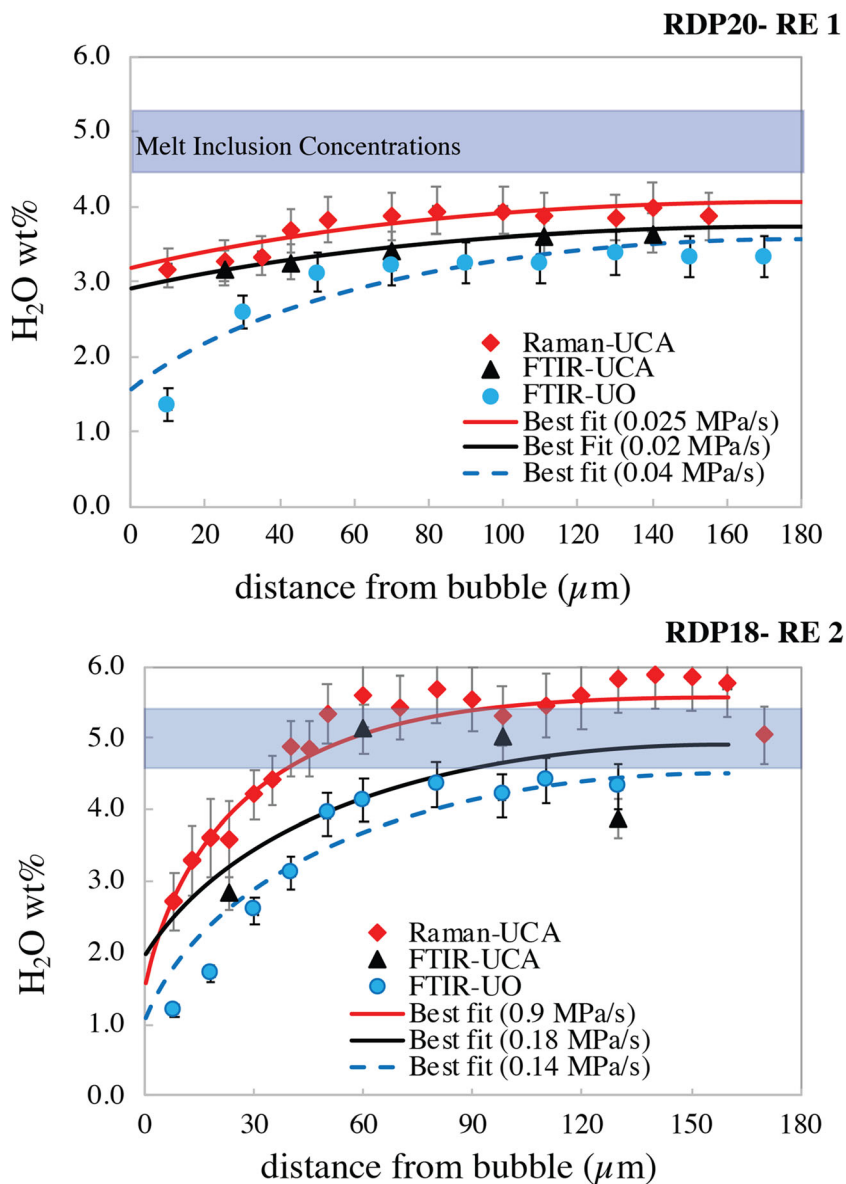
### Melt reentrant volatile profiles

Of a total of eleven measured  $\text{H}_2\text{O}$  profiles in melt reentrants, nine display gradual decreases in  $\text{H}_2\text{O}$  concentration as the transect approaches the crystal rim and the remaining two preserve slightly flatter profiles (Supplementary Figure 5). Some variabilities in  $\text{H}_2\text{O}$  concentrations and gradients are observed between the three instruments used (FTIR-UO, FTIR-UCA,

Raman-UCA), but the shape of each diffusion profile is usually similar (Fig. 7, Supplementary Table 4). Most melt reentrants measured by FTIR spectroscopy contain interior  $\text{H}_2\text{O}$  concentrations ( $\text{H}_2\text{O} = 2.0\text{--}5.0 \text{ wt\%}$ ) lower than those found in isolated melt inclusions in the same phenocryst phases ( $\text{H}_2\text{O} = 4.0\text{--}5.4 \text{ wt\%}$ , Table 2 of Druitt et al. 2016); however, some  $\text{H}_2\text{O}$  concentrations determined by Raman spectroscopy ( $\text{H}_2\text{O} = 3.2\text{--}5.9 \text{ wt\%}$ ) are higher than those found by FTIR. The absence of detectable  $\text{CO}_2$  in the melt reentrants is not surprising given the low concentrations of  $\text{CO}_2$  in isolated melt inclusions (< 200 ppm; Druitt et al. 2016) and compared to other silicic systems (Myers et al. 2018).

All 1D decompression models require an estimate of the starting pressure, initially dissolved  $\text{H}_2\text{O}$  concentration, temperature, and exsolved gas content. Models were run assuming a pre-eruptive temperature of 850 °C, a constant decompression rate, and isothermal conditions. A starting pressure (165 MPa) and  $\text{H}_2\text{O}$  concentration (5.2 wt%) were determined based on the lack of measurable  $\text{CO}_2$ , but relatively high  $\text{H}_2\text{O}$ , measured in the interiors of most melt reentrants. This pressure is broadly consistent with that estimated from melt inclusions (100–160 MPa), with  $\text{H}_2\text{O}$  concentrations representing upper end values measured from melt inclusions, but with  $\text{CO}_2$  at the lower end of the dataset (Druitt et al. 2016). To objectively choose the best-fit profile, we used an iterative grid-search function to optimize fitting of the measured profiles (Myers et al. 2018). Unlike in Myers et al. (2018), we cycled through a range of decompression rates and fragmentation pressures (pressure where diffusion ceases in the model), rather than initial gas content. This allowed us to test whether the selected best-fit fragmentation pressure shifts with time during eruption. For low- $\text{CO}_2$  systems, the selected decompression rate is less sensitive to starting gas content, so we assumed no initial exsolved gas phase.

**Fig. 7** Concentration profiles for two separate melt reentrants, RDP 18 and RDP 20, both from P1a, measured for  $\text{H}_2\text{O}$  profiles using three separate instruments (UO—University of Oregon; UCA—University of Clermont Auvergne). Each solid curve represents the best-fit decompression profile using the 1D diffusion model presented in Myers et al. (2018). For RDP 20, a fluorescent background characterizes the Raman spectra acquired at the extremities of this melt reentrant, resulting in slightly higher water contents estimated by Raman spectroscopy (see Supplementary Material for more analytical details)



It was found that for those melt reentrants where concentration profiles were measured by all three methods (eight of eleven), modeled decompression rates were fairly consistent (Fig. 5; Supplementary Figure 5). Good model fits for all profiles could be achieved using our pre-ascent storage pressure estimate of 165 MPa. Hereon, we focus on the decompression results based on the University of Oregon FTIR, where all eleven melt reentrants were measured. The resulting decompression rates range between 0.008 and 0.25  $\text{MPa s}^{-1}$ , but without any systematic variation with stratigraphic height (Table 3, Fig. 5). For those layers where multiple melt reentrants were measured and modeled (RDP18, RDP13, and RDP5), there is strong agreement between the different decompression rate estimates, especially compared to the two orders of magnitude represented by the entire dataset (Fig. 5).

## Discussion

### Time variations in plume height and mass eruption rate

Our isopleth data indicate that the plume rose from P0 to P1b, before diminishing in height after production of the pyroclastic surges of P1c (Fig. 5). Previous estimates placed the maximum plume height for phase 1 at  $36 \pm 5$  km, with a maximum eruption rate of  $1.4\text{--}4.2 \times 10^8 \text{ kg s}^{-1}$  (Sigurdsson et al. 1990, Sparks and Wilson 1990, based on the data of Bond and Sparks 1976). Our estimate of maximum plume height is lower than this (layer P1b2: plume height  $28.4 \pm 1.0$  km, mass eruption rate  $2.1 \pm 0.6 \times 10^8 \text{ kg s}^{-1}$  based on Wilson and Walker 1987), probably because we restricted sampling to a

**Table 3** Information from individual reentrant profiles used to constrain decompression rates using the 1D code described in Myers et al. (2018). All H<sub>2</sub>O and CO<sub>2</sub> measurements are based on results from FTIR measurements at the University of Oregon (see Supplementary Table 6 for results from the other techniques). For the diffusion model, starting pressure (P<sub>i</sub> = 165 MPa) and initial H<sub>2</sub>O content (5.2 wt%) are based on the

isolated melt inclusion data of Druitt et al. (2016), where final pressure (P<sub>f</sub>) is determined through the best-fit calculation. Conversion of decompression rate (dP/dt) to ascent rate assumes a magmatic pressure gradient, a magma density of 2600 kg m<sup>-3</sup>, and a magma fragmentation depth at 1 km. All concentrations of CO<sub>2</sub> were found to be below detection limits (BDL), which is ~20 ppm

Melt reentrant name	Fall layer	Length of melt reentrant (μm)	H <sub>2</sub> O interior (wt%)	BDL interior (ppm)	Interior pressure (MPa)	H <sub>2</sub> O mouth (wt%)	BDL mouth (ppm)	Pressure mouth (MPa)	dP/dt best-fit (MPa/s)	dP/dt uncertainty (MPa/s)	Ascent rate (m/s)	Best-fit fragmentation pressure (MPa)
Po-1	Po	220	3.8	0	110	2.8	0	65	0.025	0.02	1.17	50
RDP18-1	P1a1	90	4.3	0	119	2.9	0	61	0.25	0.1	11	40
RDP18-2	P1a1	160	4.3	0	119	1.5	0	18	0.14	0.05	4.9	10
RDP20-1	P1a2	180	3.4	0	80	1.4	0	16	0.04	0.02	1.5	20
RDP14-4	P1b1	320	3.2	0	72	2.31	0	40	0.008	0.001	0.3	30
RDP13-1	P1b2	80	2.9	0	60	2.6	0	50	0.012	0.02	0.56	50
RDP13-5	P1b2	80	1.9	0	28	1.67	0	23	0.01	0.01	0.37	20
RDP11-6	P1b2	110	4.2	0	115	3.3	0	76	0.1	0.1	6.3	80
RDP7-5	P1b2	140	4.3	0	119	3.8	0	97	0.02	0.02	1.43	90
RDP5-1	P1d	170	3.8	0	97	2.8	0	57	0.035	0.01	1.79	60
RDP5-2	P1d	90	2.4	0	43	1.8	0	26	0.035	0.01	1.3	20

1-m<sup>2</sup> area, whereas Bond and Sparks (1976) sampled over the entire outcrop (R.S.J. Sparks, written communication).

### Comparison of the decompression rate estimates

Calculated magma decompression rates based on vesicle number density differ by more than an order of magnitude, depending on the nucleation assumption (2–19 MPa s<sup>-1</sup>—heterogeneous or 50–450 MPa s<sup>-1</sup>—homogeneous; Fig. 5). Homogenous nucleation is commonly assumed to dominate in more evolved melts (Mangan and Sisson 2000) since silicate minerals are thought to be poor nucleation sites for vesicles (Hurwitz and Navon 1994). Much of the requirement for heterogeneous nucleation is based on the presence of Fe-Ti oxides, long established as the best nucleation site for vesicles (Hurwitz and Navon 1994). However, a review of vesicle size distributions and magma decompression rates by Shea (2017) demonstrates that the assumption of homogenous nucleation, and the resulting interfacial tension value, produces decompression estimates that are inconsistent with other rate meters, and often requires overpressures greater than the inferred depth of storage. Shea (2017) argues that heterogeneous nucleation is likely operating in all magmas (basaltic through rhyolitic), perhaps facilitated by oxide nanolites. The following lines of evidence suggest that heterogeneous nucleation occurred during ascent of the LBA magma: (1) H<sub>2</sub>O gradients measured in reentrants can be modeled by constant decompression from the storage region to the fragmentation level, requiring that diffusion to a degassing external melt was occurring early on in magma ascent (and hence that the

external melt was growing vesicles); (2) apparent nucleation of vesicles on Fe-Ti oxide grains contained within melt reentrants (Supplementary Figure 2—not evaluated for H<sub>2</sub>O profiles/decompression rate).

Even assuming heterogeneous nucleation, the decompression rates from melt reentrants (0.008 to 0.25 MPa s<sup>-1</sup>, average 0.06 MPa s<sup>-1</sup>) are 2–3 orders of magnitude lower than those based on vesicle number density (2–19 MPa s<sup>-1</sup>), although they both span about an order of magnitude. Previous workers have also noted discrepancies between the rates retrieved from melt reentrants and those from vesicles (Shea 2017; Cassidy et al. 2018). The offset can be understood by considering the kinetics of the two processes. While vesicles nucleate on timescales of seconds in response to rapid magma decompression (e.g., Toramaru 2006; Hajimirza et al. 2019; Nishiwaki and Toramaru 2019), the ability of a H<sub>2</sub>O gradient in a melt reentrant to react to external decompression is limited by the rate of H<sub>2</sub>O diffusion in melt. Melt reentrants will cease recording diffusive H<sub>2</sub>O loss if the magma decompression rate becomes too fast. Liu et al. (2007) estimate this threshold to be ~0.25 MPa s<sup>-1</sup> in silicic systems, which indeed corresponds to the uppermost decompression rates reported here and by Myers et al. (2018). While melt reentrants are unable to record decompression rates much higher than this value, vesicle number densities can record much faster rates (Shea 2017). The offset in decompression rates estimated by the two methods suggests that the decompression rate of the magma increased during ascent, from < 0.25 (recorded by melt reentrants) to ≫ 0.25 MPa s<sup>-1</sup> (recorded

by vesicles). We envisage two possible explanations, distinguishing between deeper and shallower levels of the feeder conduit.

1. *Nonlinear pressure gradient during ascent to the fragmentation level.* As the magma ascends in the feeder conduit, water diffuses from the melt into vesicles. The mixture of gas and melt is then accelerated to the surface and undergoes fragmentation. During this process, the magma can experience rapidly accelerating decompression due to: (1) increasing gas fraction as the magma degasses and the gas phase expands (i.e., mass continuity); (2) large ( $\gg$  lithostatic) nonlinear pressure gradients immediately beneath the fragmentation level due to the marked increase in melt viscosity as the dissolved water content decreases (Cashman and Scheu 2015; Gonnermann 2015) (as a silicic melt with 5 wt% water degasses to 1 wt% water, its viscosity increases by 2–3 orders of magnitude (Giordano et al. 2008; Romine and Whittington 2015); (3) rapid decompression associated with magma fragmentation. The high rates of magma decompression preceding, and accompanying, fragmentation may in some cases trigger a second vesicle nucleation event (Massol and Koyaguchi 2005; Toramaru 2006; Hamada et al. 2010; Hajimirza et al. 2019).
2. *Upwardly converging magma flow.* Accelerating magma flow may also result from changes in conduit geometry with depth beneath the volcano, for example, a feeder dike at depth focusing upwards into a narrow, shallow conduit. Syn-eruptive magma flow through a deep, dike-shaped conduit transitioning into a shallow cylindrical conduit has been called upon at a number of volcanoes, such as Montserrat in the Antilles (Costa et al. 2007) and Somma-Vesuvius in Italy (Massaro et al. 2018). The location of the vents of LBA phases P0 and P1 on the NE-SW-trending Kameni Line (Fig. 1b), a long-lived line of weakness in Santorini caldera, suggests that it is possible that the LBA magma left its upper crustal reservoir in a dike, then converged into a more cylindrical conduit at shallow levels. This is also inferred to have occurred during historical activity at Santorini (Pyle and Elliott 2006, Fig. 8). The upward focusing of magma flow from a 2-km-long dike (the deep conduit) into a 20-m-long segment of that dike (the shallow conduit) could have increased the ascent rate of the LBA magma by two orders of magnitude, providing another possible explanation of the offset between melt reentrants and vesicle number density. In this mechanism, the LBA melt reentrants would record the initial slow stage of magma ascent through the deeper feeder dike,

and vesicle number density the much faster stage of focused magma flow through the shallow conduit.

In summary, we infer that the 2–3 orders of difference between the decompression rates recorded by melt reentrants and vesicles can be attributed to the nonlinear pressure gradient associated with the fragmentation level, possibly coupled with a downward flaring of the feeder conduit. Since melt reentrants only record slower decompression conditions ( $< 0.25 \text{ MPa s}^{-1}$ ), they likely record flow during deeper magma ascent, whereas vesicle number densities are weighted towards the rapid, nonlinear decompression of faster, shallow ascent associated with fragmentation (Fig. 8; Massol and Koyaguchi 2005; Toramaru 2006; Hamada et al. 2010; Shea 2017; Hajimirza et al. 2019).

### Integration of the different parameter sets

We now compare time variations of the different eruption-intensity proxies (Fig. 5). Mass eruption rate is lowest in P0 and rises steadily to a maximum near the top of P1b, before decreasing in P1d. Decompression rate from vesicle number density mimics mass eruption rate by increasing from P0 to P1a2, being highest at the top of P1b2, then decreasing in P1d. However, it differs from mass eruption rate in that it shows a small drop from P1a2 to P1b1. Finally, decompression rate from melt reentrants increases from P0 to P1a1, then decreases markedly into P1a2 and P1b1 before rising again. Time variations of the three parameters suggests (1) magma decompression rate in the deep conduit (recorded by melt reentrants) is decoupled from mass eruption rate at the surface; (2) vesicles record rates intermediate between that in the deep conduit and the mass eruption rate; and (3) changes in decompression rate in the shallow conduit appear to lag behind those in the deep conduit (for example, the drop in decompression rate from P1a1 to P1a2 in the deep conduit occurs in vesicle number density from P1a2 to P1b1; Fig. 5).

The observed decoupling between the deep and shallow levels of the conduit may be understood if the deep conduit was a dike, as discussed earlier (Fig. 8). In eruptions fed by dikes that transition into shallow cylindrical conduits, significant decoupling of the two levels of the feeder system is possible (Costa et al. 2007; Massaro et al. 2018). The dike can act as a magmatic capacitor, storing magma (and pressure) by elastic deformation of the dike walls before conveying it to the fragmentation level in the shallow cylindrical conduit. The shallow conduit, generated by vent erosion, in turn modulates the mass eruption rate. Abrupt changes in deep conduit conditions can cause transient flow states, which, due to the high viscosities of silicic melts, can take several hours to propagate up into the shallow conduit (de' Micheli Vitturi et al. 2010). Such effects may explain why time variations in our shallow

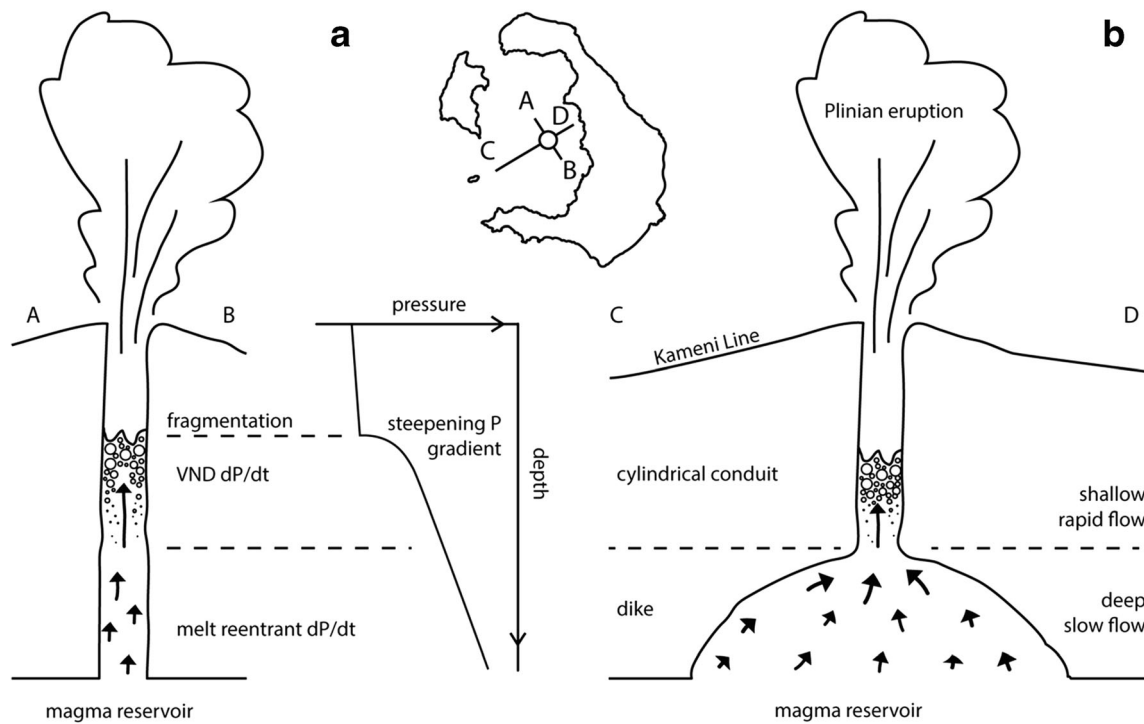


**Fig. 8** Schematic showing a snapshot in time of two possible explanations why the decompression rates recorded by melt reentrants are at least 2–3 orders of magnitude lower than those recorded by vesicle number densities. The figure shows two profiles through the LBA Plinian vent: **a** one perpendicular to the Kameni Line (profile A–B), and **b** the other parallel to it (profile C–D). The interpretation of each profile is as follows: **a** As magma ascends and degasses in the conduit, the viscosity (and hence pressure gradient) rises dramatically. Melt reentrants are

thought to record the relatively low decompression rates ( $dP/dt$ ) deep in the conduit, and vesicle number densities (VND) to record the high decompression rates associated with fragmentation. **b** An additional effect may have been that the eruption was fed through a dike along the Kameni Line, which then focussed into a cylindrical conduit at shallow levels. Due to upwardly converging flow, the decompression rates in the dike would have been slower than those in the shallow conduit

(vesicle number density–derived) decompression rate appear to be intermediate between the deep (melt reentrant–derived) decompression rate and the mass eruption rate.

It is unclear what could have caused magma ascent rate in the feeder dike to drop by over an order of magnitude during P1a1 and P1b1. Assuming that the data are representative of the magma as a whole, one possibility is that the melt reentrants are recording short-term fluctuations in deep magma decompression rate not captured by the mass eruption rate data. While mass eruption data are layer-averaged, melt reentrants are derived from individual magma parcels (pyroclasts) and may record processes taking place on shorter timescales. The bedded nature of P1a shows that eruptive conditions early on in phase 1 were unsteady, and that quasi-steady conditions were not attained until P1b. The occurrence of a coarse ash parting at the P1a–P1b boundary (Figs. 1c and 2c, d) suggests that the mass eruption rate declined greatly at this point in the eruption, as supported by the decrease in decompression rate preserved by melt reentrants and VND, although not shown by our isopleth data. This suggests that melt reentrants and vesicles, due to their ability to respond rapidly to changing decompression conditions (although on subtly different timeframes), may record changes in eruption history that

might not be recognized as significant time breaks in the field. The low decompression rates recorded by melt reentrants in P1a2 and at the base of P1b may therefore be inherited from early unsteadiness in deep magma flow as the conduit geometry evolved in response to changes in magma pressure and crustal stresses. Early transient flow and eruption unsteadiness might have been due to widening and lengthening of the deep feeder dike as the eruption gained pace, as also invoked for the Pomice di Avellino eruption of Vesuvius (Massaro et al. 2018).

### Behavior of the fragmentation level

The parameter variations in Fig. 5 offer a possible explanation for the drop in fragmentation level during P1b, as inferred from lithic data and supported by the highest melt-reentrant mouth pressures being preserved at the P1b2 level (80–90 MPa; Supplementary Figure 6). Magma fragmentation rate is controlled by a number of factors, including magma composition, volatile content, rheology, and flow rate (Cashman and Scheu 2015; Gonnermann 2015; Cassidy et al. 2018 and references therein). Neither magma composition, dissolved volatile content, nor rheology changed

significantly during the eruption (Flaherty et al. 2018). Thus, the main process causing the fragmentation level to fall throughout P1b was probably the increasing magma flow rate through the conduit. This could have increased the magma fragmentation rate by increasing the rates of strain and decompression of the magma, as well as the development of gas overpressure in the vesicles (Gonnermann 2015). In turn, this could have caused the rate of fragmentation to exceed the rate of magma supply from depth, resulting in a drop of the fragmentation level in the conduit. Indeed, the number of free crystals (relative to magma crystal content) increase upwards in fall unit P1b, which when coupled with analysis of particle populations, is consistent with increasing fragmentation rate during the Plinian eruption prior to phase P1c (Taddeucci and Wohletz 2001). The apparent decline in magma supply from the deep feeder dyke early on during P1b (as recorded by melt reentrants) may have also played a role by starving the fragmentation level of ascending magma (Fig. 5). Once the fragmentation level had dropped significantly in P1b, access of seawater to the conduit, and/or the onset of plume instabilities, caused pyroclastic surge production (P1c). This was then followed by re-establishment of shallow fragmentation (inferred by lithics) and Plinian phase P1d.

### Rapid exploitation of a pre-existing conduit system

Previous work on the opening phases of large rhyolitic eruptions (Huckleberry Ridge, Oruanui, and Bishop caldera-forming eruptions) found that melt reentrant diffusion profiles recorded at least a two-stage decompression history: (1) an initial stage of slow decompression prior to (2) a final, faster ascent associated with the explosive eruption (Myers et al. 2018). This explanation was required because measured diffusion profiles in crystals from the opening phases were best recreated using starting volatile concentrations lower than the pre-eruptive magma storage concentrations recorded by isolated melt inclusions. However, as the eruptions progressed (most notably the Bishop Tuff), the modeled starting conditions started to approach the storage concentrations, probably due to a transition from an initial, sluggish ascent to a fully developed feeder system. These observations, however, are not applicable to the LBA eruption, where all melt reentrant profiles can be reproduced using pre-eruptive storage depth as the initial condition, even in phase 0 (albeit assuming low CO<sub>2</sub>). This could suggest that either feeder development was relatively rapid in the LBA system, or that the ascending magma exploited a pre-existing zone of weakness.

Relevant to this idea is that alongside the eruption of the main rhyodacitic LBA magma, phases 0 and 1 were accompanied by a chemically and mineralogically distinct magma (preserved as microphenocryst-rich pumices) that has been interpreted previously to represent an intrusion already present beneath the Plinian vent prior to the LBA eruption (see Druitt

2014 for full data and interpretations); indeed, this other magma accounts for up to 40% of pumice discharged during phase 0. It is therefore likely that the LBA magma exploited an already existing intrusion to reach the surface, pushing out some of its contents. Furthermore, seismic tomography has imaged a vertical cylinder of low-density rock beneath Santorini caldera extended down to 3 km, which may also suggest the existence of a long-lived structural pathway that could have been exploited by the ascending LBA magma (Hooft et al. 2019).

### Conclusions

We have compared and contrasted three eruption-intensity proxies for the sub-Plinian and Plinian opening phases of the Late Bronze-Age eruption of Santorini: plume height and mass eruption rate from lithic isopleths, magma decompression rate from pumice vesicle number densities, and magma decompression rate from H<sub>2</sub>O diffusion gradients in crystal-hosted melt reentrants. The two decompression rate determinations were carried out on the same suite of pyroclasts. The aim was to obtain insight into what each technique records and detail the processes of conduit magma flow early on in a caldera-forming eruption. The main conclusions are as follows.

1. Plume heights during fallout accumulation increased from  $8.5 \pm 1.5$  to  $28.4 \pm 1$  km, then decreased to  $21.7 \pm 1.1$  km following a transient phase of pyroclastic surge emplacement. Mass eruption rate during the fallout phases is estimated to have reached  $210 \times 10^6 \text{ kg s}^{-1}$ .
2. Decompression rates estimated from vesicle number densities are 2–3 orders of magnitude higher than those from melt reentrant H<sub>2</sub>O diffusion gradients ( $0.008$  to  $0.25 \text{ MPa s}^{-1}$ ) if heterogeneous vesicle nucleation is assumed ( $2$ – $19 \text{ MPa s}^{-1}$ ), and 4 orders of magnitude higher if homogeneous nucleation is assumed ( $50$ – $450 \text{ MPa s}^{-1}$ ). Whereas melt reentrants record slow ( $< 0.25 \text{ MPa s}^{-1}$ ) magma decompression during flow deep in the conduit, vesicle number densities record much higher rates of decompression in the shallow conduit, probably due to the steep, nonlinear pressure gradients associated with magma fragmentation. Convergent flow from a dike-shaped deep conduit to a more cylindrical shallow conduit may also in part explain the high rates of magma decompression recorded by vesicles. The two methods therefore provide information on syn-eruptive magma decompression rates at different levels in the conduit.
3. The time variation of magma decompression rate in the deep conduit (recorded by melt reentrants) is decoupled from mass eruption rate at the surface, whereas that in the shallow conduit (recorded by vesicles) lies in between.

Changes in shallow decompression rate appear to lag behind those in deep decompression rate. A decrease in decompression rate preserved by melt reentrants during the transition from unsteady to steady flow may have resulted from transient flow phenomena in a deep feeder dike, possibly caused by an event of dike widening and/or lengthening.

4. Peak eruptive conditions during the Plinian phase were preceded by a fall in the fragmentation level, perhaps due to the increasing rates of shallow magma decompression and strain causing the rate of magma fragmentation to exceed that of magma supply from deeper in the conduit.
5. Melt reentrants and vesicles, due to their ability to respond rapidly to changing decompression conditions, may record changes in eruption history that might not be recognized as significant time breaks in the field.
6. The data support a previously published interpretation that the LBA magma made its way to the surface through a pre-existing zone of weakness, likely associated with an intrusion related to an earlier phase of magma movement.

**Supplementary Information** The online version contains supplementary material available at <https://doi.org/10.1007/s00445-021-01438-3>.

**Acknowledgements** The authors would like to thank Bruce Houghton for conversations surrounding isopleth/isopach data, and helpful reviews by the editor, one anonymous reviewer and Alessandro Vona that led to an improved manuscript. We also thank Christophe Constantin for thin sections, Jean-Marc Hénot for assistance with the SEM, and Erica Duncan, Emma Kerins, Megan Saalfeld, and Crystal Christensen for processing SEM images. This is Laboratory of Excellence ClerVolc Contribution Number 448.

**Funding** This work was funded through a Clermont Auvergne University Postdoctoral grant to Druitt and an NSF grant EAR-1922513 to Myers.

## References

Barberi F, Cioni R, Rosi M, Santacroce R, Sbrana A, Vecci R (1989) Magmatic and phreatomagmatic phases in explosive eruptions of Vesuvius as deduced by grain-size and component analysis of the pyroclastic deposits. *J Volcanol Geotherm Res* 38:287–307. [https://doi.org/10.1016/0377-0273\(89\)90044-9](https://doi.org/10.1016/0377-0273(89)90044-9)

Biass S, Bonadonna C (2011) A quantitative uncertainty assessment of eruptive parameters derived from tephra deposits: the example of two large eruptions of Cotopaxi volcano, Ecuador. *Bull Volcanol* 73:73–90. <https://doi.org/10.1007/s00445-010-0404-5>

Bonadonna C, Costa A (2013) Plume height, volume, and classification of explosive volcanic eruptions based on the Weibull function. *Bull Volcanol* 75:742. <https://doi.org/10.1007/s00445-013-0742-1>

Bond A, Sparks RSJ (1976) The Minoan eruption of Santorini, Greece. *J Geol Soc* 132:1–16. <https://doi.org/10.1144/gsjgs.132.1.0001>

Cadoux A, Scaillet B, Druitt TH, Deloule E (2014) Magma storage conditions of Large Plinian eruptions of Santorini volcano (Greece). *J Petrol* 55:1129–1171. <https://doi.org/10.1093/petrology/egu021>

Carey S, Sparks RSJ (1986) Quantitative models of the fallout and dispersal of tephra from volcanic eruption columns. *Bull Volcanol* 48: 109–125. <https://doi.org/10.1007/BF01046546>

Cashman KV, Scheu B (2015) Magmatic fragmentation. In: The encyclopedia of volcanoes. Academic Press, pp 459–471

Cassidy M, Manga M, Cashman K, Bachmann O (2018) Controls on explosive-effusive volcanic eruption styles. *Nat Commun* 9:2839. <https://doi.org/10.1038/s41467-018-05293-3>

Castro JM, Gardner JE (2008) Did magma ascent rate control the explosive-effusive transition at the Inyo volcanic chain, California. *Geology* 36:279. <https://doi.org/10.1130/G24453A.1>

Cioni R, Gurioli L, Sbrana A, Vougioukalakis G (2000) Precursory phenomena and destructive events related to the Late Bronze Age Minoan (Thera, Greece) and AD 79 (Vesuvius, Italy) Plinian eruptions; inferences from the stratigraphy in the archaeological areas. *Geol Soc Lond Spec Publ* 171:123–141. <https://doi.org/10.1144/GSL.SP.2000.171.01.11>

Cluzel N, Laporte D, Provost A, Kannewischer I (2008) Kinetics of heterogeneous bubble nucleation in rhyolitic melts: implications for the number density of bubbles in volcanic conduits and for pumice textures. *Contrib Mineral Petrol* 156:745–763. <https://doi.org/10.1007/s00410-008-0313-1>

Costa A, Melnik O, Sparks RSJ, Voight B (2007) Control of magma flow in dykes on cyclic lava dome extrusion. *Geophys Res Lett* 34: L02303. <https://doi.org/10.1029/2006GL027466>

Cottrell E, Gardner JE, Rutherford MJ (1999) Petrologic and experimental evidence for the movement and heating of the pre-eruptive Minoan rhyodacite (Santorini, Greece). *Contrib Mineral Petrol* 135:315–331. <https://doi.org/10.1007/s004100050514>

de' Michieli Vitturi M, Clarke AB, Neri A, Voight B (2010) Transient effects of magma ascent dynamics along a geometrically variable dome-feeding conduit. *Earth Planet Sci Lett* 295:541–553. <https://doi.org/10.1016/j.epsl.2010.04.029>

Degruyter W, Bachmann O, Burgisser A, Manga M (2012) The effects of outgassing on the transition between effusive and explosive silicic eruptions. *Earth Planet Sci Lett* 349–350:161–170. <https://doi.org/10.1016/j.epsl.2012.06.056>

Doocy S, Daniels A, Dooling S (2013. Edition 1.) Gorokhovich Y. The human impact of volcanoes: a historical review of events 1900–2009 and systematic literature review. *PLOS Curr Disasters*. <https://doi.org/10.1371/currents.dis.841859091a706efebf8a30f4ed7a1901>

Druitt TH (2014) New insights into the initiation and venting of the Bronze-Age eruption of Santorini (Greece), from component analysis. *Bull Volcanol* 76:794. <https://doi.org/10.1007/s00445-014-0794-x>

Druitt TH, Edwards L, Mellors RM et al (1999) Santorini volcano. *Geol Soc Mem* 19

Druitt TH, Mercier M, Florentin L, Deloule E, Cluzel N, Flaherty T, Médard E, Cadoux A (2016) Magma storage and extraction associated with plinian and interplinian activity at Santorini Caldera (Greece). *J Petrol* 57:461–494. <https://doi.org/10.1093/petrology/egw015>

Flaherty T, Druitt TH, Tuffen H, Higgins MD, Costa F, Cadoux A (2018) Multiple timescale constraints for high-flux magma chamber assembly prior to the Late Bronze Age eruption of Santorini (Greece). *Contrib Mineral Petrol* 173:75. <https://doi.org/10.1007/s00410-018-1490-1>

Giachetti T, Druitt TH, Burgisser A, Arbaret L, Galven C (2010) Bubble nucleation, growth and coalescence during the 1997 Vulcanian explosions of Soufrière Hills Volcano, Montserrat. *J Volcanol Geotherm Res* 193:215–231. <https://doi.org/10.1016/j.jvolgeores.2010.04.001>

Giordano D, Russell JK, Dingwell DB (2008) Viscosity of magmatic liquids: a model. *Earth Planet Sci Lett* 271:123–134. <https://doi.org/10.1016/j.epsl.2008.03.038>

Gonnermann HM (2015) Magma fragmentation. *Annu Rev Earth Planet Sci* 43:431–458. <https://doi.org/10.1146/annurev-earth-060614-105206>

Hajimirza S, Gonnermann HM, Gardner JE, Giachetti T (2019) Predicting homogeneous bubble nucleation in rhyolite. *J Geophys Res Solid Earth* 124:2395–2416. <https://doi.org/10.1029/2018JB015891>

Hamada M, Laporte D, Cluzel N, Koga KT, Kawamoto T (2010) Simulating bubble number density of rhyolitic pumices from Plinian eruptions: constraints from fast decompression experiments. *Bull Volcanol* 72:735–746. <https://doi.org/10.1007/s00445-010-0353-z>

Heiken G, McCoy F (1990) Precursory activity to the Minoan eruption, Thera, Greece. In: Hardy DA (ed) *Thera and the Aegean World III*, vol 2. Thera Foundation, London, pp 13–18

Heiken G, McCoy F Jr (1984) Caldera development during the Minoan eruption, Thira, Cyclades, Greece. *J Geophys Res* 89:8441–8462

Hildreth W, Drake R (1992) Volcanic Quizapu, Chilean Andes. *Bull Volcanol* 54:93–125

Hooft EEE, Heath BA, Toomey DR, Paulatto M, Papazachos CB, Nomikou P, Morgan JV, Warner MR (2019) Seismic imaging of Santorini: subsurface constraints on caldera collapse and present-day magma recharge. *Earth Planet Sci Lett* 514:48–61. <https://doi.org/10.1016/j.epsl.2019.02.033>

Houghton BF, Carey RJ, Cashman KV, Wilson CJ, Hobden BJ, Hammer JE (2010) Diverse patterns of ascent, degassing, and eruption of rhyolite magma during the 1.8 ka Taupo eruption, New Zealand: evidence from clast vesicularity. *J Volcanol Geotherm Res* 195:31–47

Houghton BF, Carey RJ, Rosenberg MD (2014) The 1800a Taupo eruption: “III wind” blows the ultraplumian type event down to Plinian. *Geology* 42:459–461. <https://doi.org/10.1130/G35400.1>

Hurwitz S, Navon O (1994) Bubble nucleation in rhyolitic melts: experiments at high pressure, temperature, and water content. *Earth Planet Sci Lett* 122:267–280. [https://doi.org/10.1016/0012-821X\(94\)90001-9](https://doi.org/10.1016/0012-821X(94)90001-9)

Kaviris G, Papadimitriou P, Kravvariti P, Kapetanidis V, Karakonstantis A, Voulgaris N, Makropoulos K (2015) A detailed seismic anisotropy study during the 2011–2012 unrest period in the Santorini Volcanic Complex. *Phys Earth Planet Inter* 238:51–88. <https://doi.org/10.1016/j.pepi.2014.11.002>

Klug C, Cashman KV (1996) Permeability development in vesiculating magmas: implications for fragmentation. *Bull Volcanol* 58:87–100. <https://doi.org/10.1007/s004450050128>

Liu Y, Anderson AT, Wilson CJN (2007) Melt pockets in phenocrysts and decompression rates of silicic magmas before fragmentation. *J Geophys Res* 112:B06204. <https://doi.org/10.1029/2006JB004500>

Lloyd AS, Ruprecht P, Hauri EH, Rose W, Gonnermann HM, Plank T (2014) NanoSIMS results from olivine-hosted melt embayments: magma ascent rate during explosive basaltic eruptions. *J Volcanol Geotherm Res* 283:1–18. <https://doi.org/10.1016/j.jvolgeores.2014.06.002>

Mangan M, Sisson T (2000) Delayed, disequilibrium degassing in rhyolite magma: decompression experiments and implications for explosive volcanism. *Earth Planet Sci Lett* 183:441–455. [https://doi.org/10.1016/S0012-821X\(00\)00299-5](https://doi.org/10.1016/S0012-821X(00)00299-5)

Martel C, Iacono-Marziano G (2015) Timescales of bubble coalescence, outgassing, and foam collapse in decompressed rhyolitic melts. *Earth Planet Sci Lett* 412:173–185. <https://doi.org/10.1016/j.epsl.2014.12.010>

Mason BG, Pyle DM, Oppenheimer C (2004) The size and frequency of the largest explosive eruptions on Earth. *Bull Volcanol* 66:735–748. <https://doi.org/10.1007/s00445-004-0355-9>

Massaro S, Costa A, Sulpizio R (2018) Evolution of the magma feeding system during a Plinian eruption: the case of Pomici di Avellino eruption of Somma–Vesuvius, Italy. *Earth Planet Sci Lett* 482: 545–555. <https://doi.org/10.1016/j.epsl.2017.11.030>

Massol H, Koyaguchi T (2005) The effect of magma flow on nucleation of gas bubbles in a volcanic conduit. *J Volcanol Geotherm Res* 143: 69–88. <https://doi.org/10.1016/j.jvolgeores.2004.09.011>

Mastin LG, Guffanti M, Servranckx R, Webley P, Barsotti S, Dean K, Durant A, Ewert JW, Neri A, Rose WI, Schneider D, Siebert L, Stunder B, Swanson G, Tupper A, Volentik A, Waythomas CF (2009) A multidisciplinary effort to assign realistic source parameters to models of volcanic ash-cloud transport and dispersion during eruptions. *J Volcanol Geotherm Res* 186:10–21. <https://doi.org/10.1016/j.jvolgeores.2009.01.008>

Miller CF, Wark DA (2008) Supervolcanoes and their explosive supereruption. *Elements* 4:11–15. <https://doi.org/10.2113/GSELEMENTS.4.1.11>

Mourtada-Bonnefond CC, Laporte D (2004) Kinetics of bubble nucleation in a rhyolitic melt: an experimental study of the effect of ascent rate. *Earth Planet Sci Lett* 218:521–537. [https://doi.org/10.1016/S0012-821X\(03\)00684-8](https://doi.org/10.1016/S0012-821X(03)00684-8)

Myers ML, Wallace PJ, Wilson CJN, Morter BK, Swallow EJ (2016) Prolonged ascent and episodic venting of discrete magma batches at the onset of the Huckleberry Ridge supereruption, Yellowstone. *Earth Planet Sci Lett* 451:285–297. <https://doi.org/10.1016/j.epsl.2016.07.023>

Myers ML, Wallace PJ, Wilson CJN, Watkins JM, Liu Y (2018) Ascent rates of rhyolitic magma at the onset of three caldera-forming eruptions. *Am Mineral* 103:952–965. <https://doi.org/10.2138/am-2018-6225>

Nishiwaki M, Toramaru A (2019) Inclusion of viscosity into classical homogeneous nucleation theory for water bubbles in silicate melts: reexamination of bubble number density in ascending magmas. *J Geophys Res Solid Earth* 124:8250–8266. <https://doi.org/10.1029/2019JB017796>

Pyle DM, Elliott JR (2006) Quantitative morphology, recent evolution, and future activity of the Kameni Islands volcano, Santorini, Greece. *Geosphere* 2:253. <https://doi.org/10.1130/GES00028.1>

Romine WL, Whittington AG (2015) A simple model for the viscosity of rhyolites as a function of temperature, pressure and water content. *Geochim Cosmochim Acta* 170:281–300. <https://doi.org/10.1016/j.gca.2015.08.009>

Shea T (2017) Bubble nucleation in magmas: a dominantly heterogeneous process? *J Volcanol Geotherm Res* 343:155–170. <https://doi.org/10.1016/j.jvolgeores.2017.06.025>

Shea T, Houghton BF, Gurioli L, Cashman KV, Hammer JE, Hobden BJ (2010) Textural studies of vesicles in volcanic rocks: an integrated methodology. *J Volcanol Geotherm Res* 190:271–289. <https://doi.org/10.1016/j.jvolgeores.2009.12.003>

Sigurdsson H, Carey S, Devine, JD (1990) Assessment of mass, dynamics and environmental effects of the Minoan eruption of Santorini volcano. *Thera and the Aegean world III* 2:100–112

Sparks RSJ, Wilson CJN (1990) The Minoan deposits: a review of their characteristics and interpretation. In: Hardy DA (ed) *Thera and the Aegean World III*, vol 2. Thera Foundation, London, pp 89–99

Sulpizio R, Cioni R, Di Vito MA et al (2010) The Pomici di Avellino eruption of Somma–Vesuvius (3.9 ka bp). Part I: stratigraphy, compositional variability and eruptive dynamics. *Bull Volcanol* 72:539–558. <https://doi.org/10.1007/s00445-009-0339-x>

Taddeucci J, Wohletz KH (2001) Temporal evolution of the Minoan eruption (Santorini, Greece), as recorded by its Plinian fall deposit and interlayered ash–ow beds. *J Volcanol Geotherm Res* 19

Thomas N, Jaupart C, Vergniolle S (1994) On the vesicularity of pumice. *J Geophys Res: Solid Earth* 99(B8):15633–15644

Toramaru A (2006) BND (bubble number density) decompression rate meter for explosive volcanic eruptions. *J Volcanol Geotherm Res* 154:303–316. <https://doi.org/10.1016/j.jvolgeores.2006.03.027>

Wilson CJN, Houghton BF (1990) Eruptive mechanisms in the Minoan eruption: evidence from pumice vesicularity. *Thera and the Aegean world III* 2:122–128

Wilson L, Walker GPL (1987) Explosive volcanic eruptions-VI. Ejecta dispersal in plinian eruptions: the control of eruption conditions and atmospheric properties. *Geophys J Int* 89:657–679. <https://doi.org/10.1111/j.1365-246X.1987.tb05186.x>

Woods AW, Koyaguchi T (1994) Transitions between explosive and effusive eruptions of silicic magmas. *Nature* 370:641–644. <https://doi.org/10.1038/370641a0>

Zhang Y, Xu Z, Zhu M, Wang H (2007) Silicate melt properties and volcanic eruptions: SILICATE MELT PROPERTIES. *Rev Geophys* 45. <https://doi.org/10.1029/2006RG000216>